Synthesis of Porous ZnS:Ag$_2$S Nanosheets by Ion Exchange for Photocatalytic H$_2$ Generation

Xia Yang,[†] Hongtao Xue,[†] Jun Xu,[†,‡] Xing Huang,[†,§] Jie Zhang,[†] Yong-Bing Tang,[†] Tsz-Wai Ng,[†] Hoi-Lun Kwong,[‖] Xiang-Min Meng,[§] and Chun-Sing Lee*,[†]

[†]Center of Super-Diamond and Advanced Films (COSDAF) and Department of Physics and Materials Science, City University of Hong Kong, Hong Kong SAR, and City University's Shenzhen Research Institute, Hong Kong, China

[‡]Schools of Electronic Science and Applied Physics, Hefei University of Technology, Hefei, Anhui, P. R. China

[‖]Department of Biology and Chemistry, City University of Hong Kong, Hong Kong, China

[§]Key Laboratory of Photochemical Conversion and Optoelectronic Materials, Technical Institute of Physics and Chemistry, Chinese Academy of Sciences, Beijing 100190, P. R. China

S **Supporting Information**

ABSTRACT: ZnS:Ag$_2$S porous nanostructures are prepared by a simple ion-exchange route using ZnS nanosheets as sacrificial templates. In solutions of different Ag ion concentrations, ZnS nanosheets are partially converted to Ag$_2$S, resulting in porous ZnS:Ag$_2$S nanosheet composites with different pore sizes. With the Ag$_2$S nanocrystals playing the role of hole scavengers, the porous nanosheets exhibit a high photocatalytic H$_2$ generation rate of 104.9 μmol/h/g without using any noble metal cocatalyst.

KEYWORDS: porous nanosheet, ion exchange, hole scavenger, photocatalytic H$_2$ generation
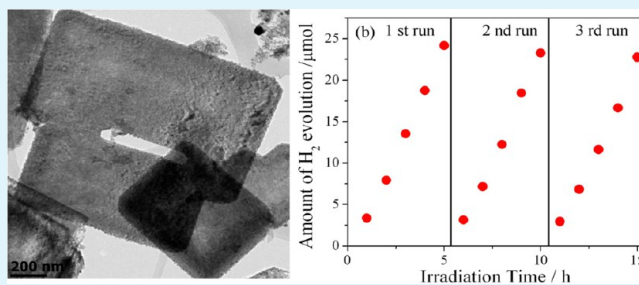
1. INTRODUCTION

Photocatalytic H$_2$ generation has attracted much attention because of the increasing demand for clean energy.[1−6] In addition to exploring new high-performance catalysts, strategies for enhancing the separation of photoexcited electron and hole pairs are also an important research topic.[7−12] An effective approach for enhancing charge separation is the use of a suitable cocatalyst.[13,14] For example, NiO,[15] MoS$_2$,[16,17] platinum,[18,19] palladium,[20] carbon nanotubes,[21] graphene,[22−25] etc., have been used as cocatalysts to assist electron transfer from the catalyst to protons with much success. While effective transport away of holes from the excitation site is also important, there are so far fewer reports on cocatalysts that assist hole transfer.[26] Thus, it is highly desirable to develop more high-performance cocatalysts capable of enhancing hole transfer.

The ion-exchange method is a versatile materials synthesis approach based on the difference in the solubility constants (K_{sp}).[27,28] Han et al. synthesized a CuS mesostructure by cation exchange of CdS and kept its original morphology.[29] Cu$_2$S are reported to be selectively converted to CdS or PbS.[30] Our group used the ion-exchange approach to convert ZnO nanorods to arrays of ZnO/CuSe, ZnO/CuInSe$_2$, ZnO/ZnSe, and ZnO/Zn$_x$Cd$_{1−x}$Se core/shell nanocables.[31,32] ZnS is a potential material for photocatalytic H$_2$ generation because of the more negative potential of its conduction band (CB) than the reduction potential of the H$^+$/H$_2$ hydrogen electrode. ZnS

has a K_{sp} of $3.0 \times 10^{−25}$, so it can be converted to materials with smaller K_{sp} values.[33] Yu et al. used monodispersed ZnS solid spheres as precursors and obtained CuS/ZnS nanocomposites via the ion-exchange method.[34] Zhang et al. and Gong et al. prepared Cd$_x$Zn$_{1−x}$S and CuS/ZnS nanostructures for respectively obtaining new small-band-gap materials and introducing cocatalysts to enhance the photocatalytic rate.[35,36] ZnS−Ag$_2$S nanoparticles, matchstick-shaped structures, and microspheres have been reported for their optical and photodegradation properties.[37−39] In this study, we prepared porous nanocomposite of ZnS:Ag$_2$S by thermal decomposition of a ZnS−organic precursor and simultaneous ion exchange. The organic component in the ingredient leads directly to the formation of a porous nanostructure, which extensively increases the surface area. Moreover, with different amounts of Ag$^+$, the composites exhibit different pore sizes. These porous nanosheet structures have large surface areas for contact with the solution to generate more active sites, which is beneficial for enhancing the photocatalytic H$_2$ evolution rate. With suitable amounts of Ag$_2$S nanocrystals, which act as hole scavengers, the porous composite nanosheet shows excellent performance for photocatalytic H$_2$ evolution. This work demonstrates that the application of Ag$_2$S as a cocatalyst for
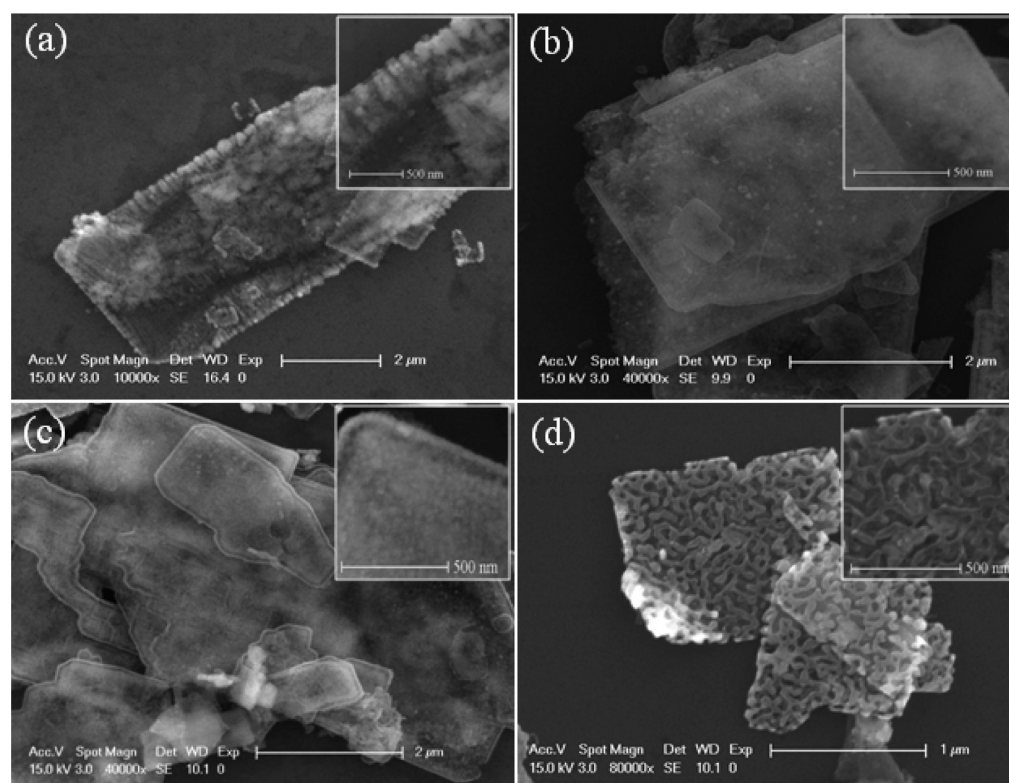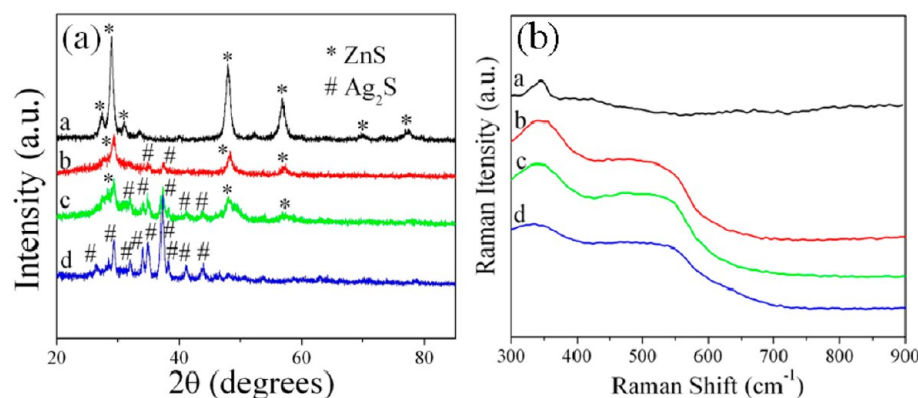
Figure 1. Products after reacting ZnS(en)$_{0.5}$ nanosheets with (a) 0, (b) 0.01, (c) 0.02, and (d) 0.08 g of AgNO$_3$, respectively. The insets of parts a–d are SEM images of higher magnification.

Figure 2. (a) XRD patterns and (b) Raman spectra of the structures after reacting ZnS(en)$_{0.5}$ nanosheets with (a) 0, (b) 0.01, (c) 0.02, and (d) 0.08 g of AgNO$_3$, respectively.

assisting hole transfer is an effective way of enhancing the photocatalytic activity of ZnS.

2. EXPERIMENTAL SECTION

2.1. Synthesis of Photocatalysts. *Preparation of Porous ZnS and ZnS:Ag$_2$S Nanosheets.* ZnS(en)$_{0.5}$ precursors were prepared according to the literature,[40] as illustrated in the Supporting Information (SI). A total of 0.04 g of the white powder precursor was dispersed in 15 mL of distilled water (four samples). Then 0, 0.01, 0.02, and 0.08 g of AgNO$_3$ were added (hereafter, samples prepared as such are respectively referred to as ZnS, ZnS:Ag$_2$S-1, ZnS:Ag$_2$S-2, and ZnS:Ag$_2$S-8). The four mixtures were then loaded into autoclaves (25 mL) and maintained at 120 °C for 12 h. After cooling, the products were sequentially washed with distilled water and absolute ethanol several times and then dried under vacuum. Finally, the products were annealed in nitrogen gas at 400 °C for 2 h.

2.2. Sample Characterization. The as-prepared samples were characterized with scanning electron microscopy (SEM) and transmission electron microscopy (TEM) with a Philips XL30 FEG scanning electron microscope and a Philips CM200 FEG transmission electron microscope (operated at 200 kV), respectively. X-ray diffraction (XRD) measurements were carried out with a Siemens D-500 diffractometer with Cu Kα radiation. Absorption spectra were recorded with a Lambda-750 UV–vis–near-IR (NIR) spectrophotometer.

2.3. Photocatalytic Test. Photocatalytic H$_2$ generation performances of the synthesized nanostructures were measured in a closed gas circulation system equipped with a top-irradiation Pyrex cell reactor. A 300 W xenon lamp was used as the light source. The reactor was first loaded with 100 mL of an aqueous solution of 0.1 M Na$_2$S and 0.1 M Na$_2$SO$_3$ as sacrificial reagents and 8 g of NaOH for enhancing the photocatalytic efficiency.[41] A total of 0.05 g of each photocatalyst sample was then respectively loaded into the reactor under magnetic

stirring. The amount of H_2 generated was determined by gas chromatography (TECHCOMP GC7900, nitrogen carrier) every 1 h. To measure the apparent quantum efficiency (AQE), a 350 nm band-pass filter was used to produce monochromatic light. The intensity of incident light was measured by a spectroradiometer. The AQE was calculated with the following equation:

$$AQE = 2N(H_2)/N(photons) \times 100\%$$

$N(H_2)$ = molecular number of generated H_2 per second, and $N(photons)$ = number of incident photons per second.

2.4. Morphology, Structure, and Composition. Figure S1 in the SI shows SEM and TEM images of the $ZnS(en)_{0.5}$ precursors, which are in the shape of nanosheets of about 100 nm thick (see nanosheets with an edge-on orientation in the inset of Figure S1a in the SI). The XRD pattern in the inset of Figure S1b in the SI is consistent with that in the literature.[40]

$ZnS(en)_{0.5}$ precursors can be converted to ZnS via hydrothermal reaction according to the literature.[42] Figure 1a is the product after hydrothermal treatment of the precursor at 120 °C. We can see that the surface of the nanosheets becomes rough, which is caused by the loss of the organic component at high temperatures. As shown in Figure 2a (curve a), the precursor is converted to hexagonal ZnS (JCPDF 36-1450, marked with *). Parts b−d of Figure 1 show the structures of the samples $ZnS:Ag_2S$-1, $ZnS:Ag_2S$-2, and $ZnS:Ag_2S$-8. For the samples $ZnS:Ag_2S$-1 and $ZnS:Ag_2S$-2 (Figure 1b,c), the nanosheet appears to be decorated with many fine particles (insets of Figure 1b,c). Curve b in Figure 2a shows that there is a small amount of Ag_2S (JCPDF 14-0072, marked with #) in the sample $ZnS:Ag_2S$-1. This is due to the fact that Ag_2S has a smaller K_{sp} (6.7×10^{-50}) than ZnS (3.0×10^{-25}). The Ag ion replaces the Zn ion in ZnS upon immersion in a Ag^+ solution. Compared with the other samples, $ZnS:Ag_2S$-8 (Figure 1d) shows the roughest surface. It appears that the sample is full of 3D interconnected grooves. On the other hand, as the amount of Ag^+ ion increases, the XRD peak intensity of ZnS decreases, while the peaks of Ag_2S become more obvious (curve c, Figure 2a). From curve d of Figure 2a, no peaks of ZnS can be found and the sample is mostly Ag_2S. It is considered that during the Zn−Ag ion-exchange process, there is a diffusion couple, which can lead to the formation of more pores via the nanoscale Kirkendall effect.[43−45] Thus, the amount of pore and roughness increases as the Ag^+ concentration increases.

Raman spectroscopy was carried out (Figure 2b) to give further information on the composition of each sample. Curve a of Figure 2b shows a peak at 350 cm^{-1}, which is attributed to ZnS obtained from the precursors.[46] Curves b and c are Raman spectra of $ZnS:Ag_2S$-1 and $ZnS:Ag_2S$-2, respectively. In addition to the peak of ZnS, we can also find the peak of Ag_2S at 560 cm^{-1}.[33] From curve d for $ZnS:Ag_2S$-8, both characteristic peaks of ZnS and Ag_2S can be observed. This suggests that, although peaks from the ZnS phase are indistinguishable in the XRD pattern for $ZnS:Ag_2S$-8 (curve d of Figure 2a), ZnS has not been completely converted to Ag_2S.

Table 1 shows the energy-dispersive X-ray spectroscopy (EDS) measurements of the four samples (spectra shown in Supporting Information figure S2). Ag content in the composite nanosheet increases with the amount of $AgNO_3$ used in the ingredient. For the sample $ZnS:Ag_2S$-8, the ratio of Zn/Ag is about 0.2. This confirms the XRD and the Raman results that most ZnS has been converted to Ag_2S. Figure S3a is a SEM image of the $ZnS:Ag_2S$-2 nanostructure and Figure 3b-3d are the corresponding Zn, Ag, S elemental mapping,

Table 1. Composition of the Nanostructures

| material	element (atom %)		
	Zn	Ag	S
ZnS	54	0	46
$ZnS:Ag_2S$-1	43	12	45
$ZnS:Ag_2S$-2	33	26	41
$ZnS:Ag_2S$-8	9	50	41

respectively, which reveal their homogeneous distributions in the porous nanosheets.
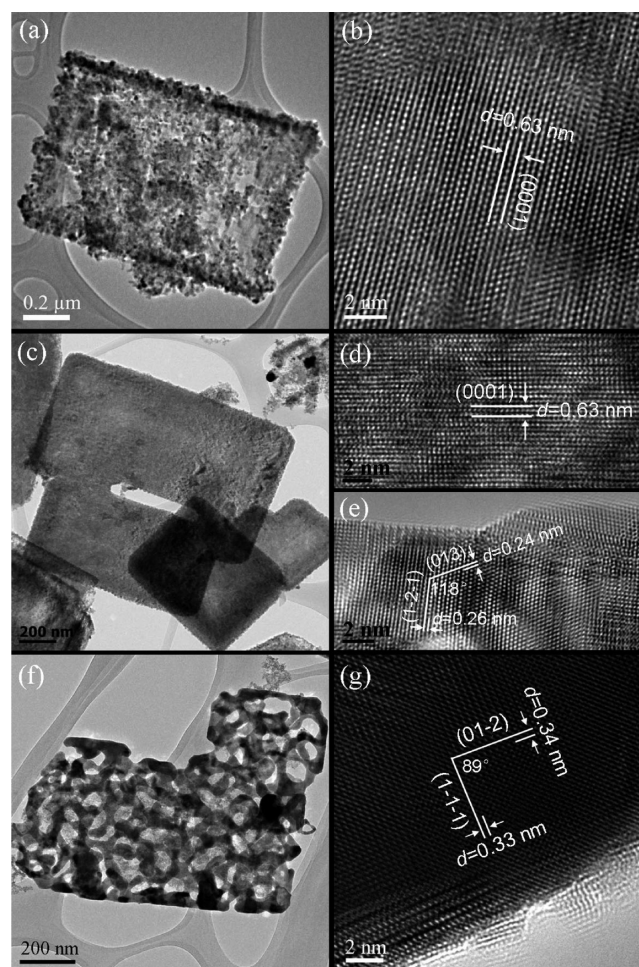
Figure 3. TEM and HRTEM images of (a and b) ZnS, (c−e) $ZnS:Ag_2S$-2 nanostructure, and (f and g) $ZnS:Ag_2S$-8 nanostructure.

Figure 3a shows a TEM image of the ZnS nanosheets obtained from hydrothermal treatment of the precursor without any $AgNO_3$. It is considered that, during the hydrothermal reaction, the organic component of the precursor is driven out of the nanosheet, leaving behind a porous structure while preserving the overall nanosheet morphology. A corresponding high-resolution TEM (HRTEM) image of the sample is shown in Figure 3b, in which the marked d spacing of 0.63 nm matches well to the (0001) lattice fringes of the hexagonal structured ZnS. Figure 3c shows a TEM image of the sample $ZnS:Ag_2S$-2 obtained by reaction of the precursor with a medium amount of $AgNO_3$. HRTEM images (Figure 3d,e) of the samples show the coexistence of both the ZnS and Ag_2S phases. While the lattice fringe in Figure 3d of 0.63 nm matches well with the lattice spacing of the (0001) plane of hexagonal ZnS, lattice fringes in Figure 3e with spacings of 0.26 and 0.24 nm correspond to the (1−2−1) and (013) planes of monoclinic Ag_2S. With the largest amount of Ag^+ in the ingredient (sample $ZnS:Ag_2S$-8), the obtained nanosheets have much larger pore sizes (Figure 3f). Because of the higher amounts of Ag ions more active sites will be introduced for ion-exchange reaction, so more pores and surface with higher roughness will be generated. A corresponding HRTEM image (Figure 3g) clearly shows lattice spacings of 0.33 and 0.34 nm with an angle of 89°, in good agreement to the (01−2) and (1−1−1) planes of monoclinic Ag_2S.

2.5. Optical Properties. Figure 4 shows UV−vis−NIR spectra of the nanostructures. The ZnS nanosheets (curve a) exhibit an absorption peak at about 330 nm in the UV region. Curves b−d
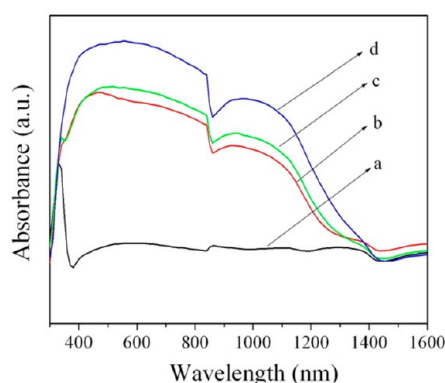
Figure 4. UV−vis−NIR spectra of (a) ZnS, (b) ZnS:Ag$_2$S-1 nanostructure, (c) ZnS:Ag$_2$S-2 nanostructure, and (d) ZnS:Ag$_2$S-8 nanostructure.

show absorption spectra of ZnS:Ag$_2$S-1, ZnS:Ag$_2$S-2, and ZnS:Ag$_2$S-8, respectively. Because of the existence of a small band gap of Ag$_2$S (0.92 eV), the nanostructures exhibit absorbance extending to the NIR region. The edges at around 850 nm are due to switching of the light source in the Lambda-750 UV−vis−NIR spectrophotometer. We have confirmed with another instrument that the samples do not have any peaks or valleys at this region.

2.6. Surface Area and Pore Size. Table 2 shows the Brunauer−Emmett−Teller (BET) surface areas and average pore sizes of different

Table 2. BET Surface Areas and Average Pore Sizes of Different Structures

	BET surface area (m^2/g)	average pore size (nm)
ZnS	36.9	11.4
ZnS:Ag$_2$S-1	33.9	10.6
ZnS:Ag$_2$S-2	250.6	2.6
ZnS:Ag$_2$S-8	1.2	15.6

structures. From the results, the BET surface areas of ZnS, ZnS:Ag$_2$S-1, ZnS:Ag$_2$S-2, and ZnS:Ag$_2$S-8 are 36.9, 33.9, 250.6, and 1.2 m^2/g, respectively. It can be seen that, although the ZnS-Ag$_2$S-8 has the largest pore size of 15.6 nm, it has the smallest surface area. The ZnS:Ag$_2$S-2 sample has the smallest pore size and the largest surface area because of the suitable amount of Ag ions.

2.7. Photocatalytic Activity. Figure 5a shows the photocatalytic H$_2$ generation performance of the nanostructures irradiated with a 300 W xenon lamp. Na$_2$S and Na$_2$SO$_3$ were added as sacrificial agents that consume the photogenerated holes from the photocatalytic surface. From curve a, the ZnS porous nanosheets exhibit a H$_2$ generation rate of 13.3 μmol/h/g. With the coexistence of Ag$_2$S, samples ZnS:Ag$_2$S-1 (curve b) and ZnS:Ag$_2$S-2 (curve c) show better H$_2$ generation rates of 56.2 and 104.9 μmol/h/g, respectively. This confirms the enhancement effects of the Ag$_2$S cocatalyst. However, when most ZnS is converted to Ag$_2$S (curve d), the ZnS:Ag$_2$S-8 sample shows the lowest H$_2$ generation rate. Because the CB level of Ag$_2$S is lower than the level of the reduction potential of H$^+$/H$_2$ (0 V vs normal hydrogen electrode), it cannot reduce H$^+$ to generate H$_2$ on itself.[9,47] Thus, when most of the photoactive ZnS is converted to Ag$_2$S, there is a small amount of material useful for generating H$_2$. It is considered that the high performance of ZnS:Ag$_2$S-2 is due to the optimum amount of Ag$_2$S and the porous nanostructure. The AQE of ZnS:Ag$_2$S-2 is 1.2% for H$_2$ evolution at an incident wavelength of 350 nm. To confirm the stability of the catalyst, the photocatalytic reaction of ZnS:Ag$_2$S-2 was tested for another two runs. After the first run for 5 h, accumulated H$_2$ was pumped out. Before the second or third run, an additional amount of Na$_2$S and Na$_2$SO$_3$ was added to replace the consumed sacrificial reagents. As shown in Figure 5b, the catalyst in the second and third runs did not exhibit any significant loss of activity compared with that of the first run. The morphology of ZnS:Ag$_2$S-2 after testing is shown
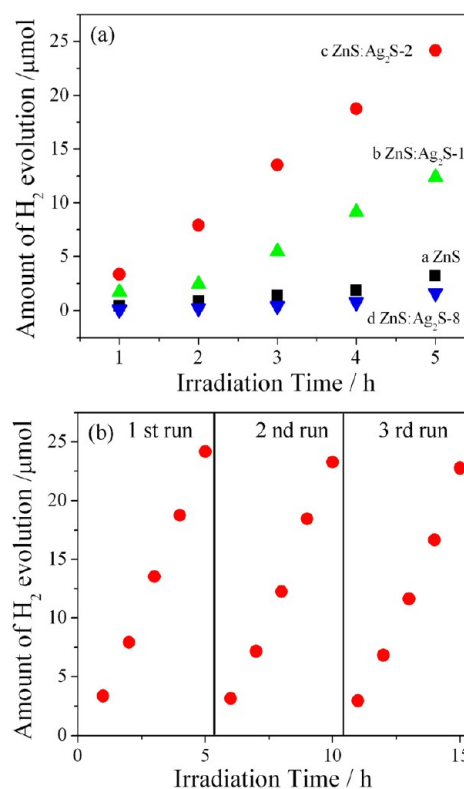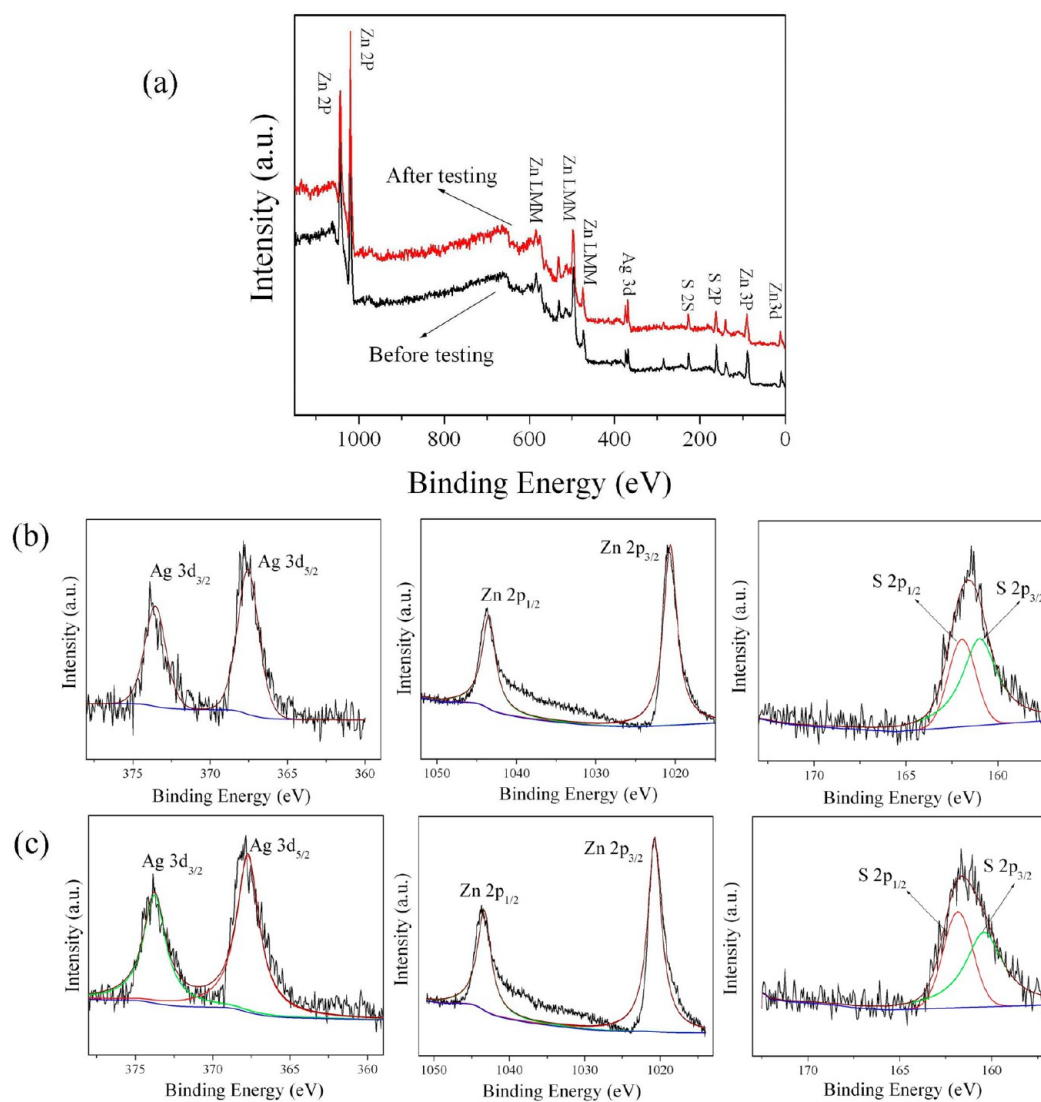

Figure 5. (a) Photocatalytic H$_2$ evolution of ZnS (curve a), ZnS:Ag$_2$S-1 (curve b), ZnS:Ag$_2$S-2 (curve c), and ZnS:Ag$_2$S-8 (curve d) porous nanostructures. (b) Stability of ZnS:Ag$_2$S-2. Light source: 300 W xenon lamp.

in Figure S4 in the SI, also suggesting that the structure of the catalyst has no obvious difference of the original morphology (Figure 1c). These results indicate that ZnS:Ag$_2$S-2 shows good stability during photocatalytic H$_2$ production.

Surface information on the ZnS:Ag$_2$S-2 catalyst was also characterized by X-ray photoelectron spectrometry (XPS) before and after photocatalytic reaction (Figure 6). It is obviously seen that, in Figure 6a, only elements of Zn, Ag, and S can be found in spectra of the catalyst before and after testing, and no other impurities were detectable. In parts b (before photocatalytic testing) and c (after photocatalytic testing) of Figure 6, the energy peaks of Ag 3d, Zn 2p, and S 2p can be observed and are almost in the same positions. The peaks at 373.6 and 367.4 eV are assigned to Ag 3d$_{3/2}$ and Ag 3d$_{5/2}$ of Ag$^+$ ions in Ag$_2$S, respectively. The Zn 2p$_{1/2}$ and Zn 2p$_{3/2}$ peaks at binding energies of 1043.5 and 1020.6 eV are assigned to Zn^{2+}. The spectra of S 2p$_{1/2}$ and S 2p$_{3/2}$ are both located at binding energies of 161.8 and 160.4 eV before and after photocatalytic testing. These results indicate that the components of ZnS:Ag$_2$S-2 have good stability after long time irradiation.

Figure 7 is a schematic diagram of the porous ZnS:Ag$_2$S nanostructures for H$_2$ evolution. When the photocatalyst is irradiated, electrons and holes would be generated. Because the CB and valence band (VB) energy levels of Ag$_2$S are bracketed by those of ZnS, both electrons and holes will be transferred to Ag$_2$S. On the one hand, electrons transferred to Ag$_2$S cannot generate H$_2$ because of the lower CB of Ag$_2$S than that of the reduction potential of H$^+$/H$_2$. So, Ag$_2$S can neither generate H$_2$ nor pass electrons from its VB to H$^+$. On the other hand, electrons from ZnS will react with protons in the water and generate H$_2$. On the other side of the catalyst, holes will transfer to Ag$_2$S on the nanosheets, which will promote carrier separation, and Ag$_2$S acts as an oxidation site. Thus, it is reasonable to consider that the better performance of the ZnS:Ag$_2$S composite is due to enhanced hole transfer via its shallower VB edge of Ag$_2$S. So, with a large surface area and a suitable amount of Ag$_2$S, the ZnS:Ag$_2$S-2 nanosheets show

Figure 6. (a) XPS spectra of ZnS:Ag$_2$S-2 nanostructures before and after photocatalytic H$_2$ evolution. XPS spectra of Ag 3d, Zn 2p, and S 2p (b) before and (c) after testing.
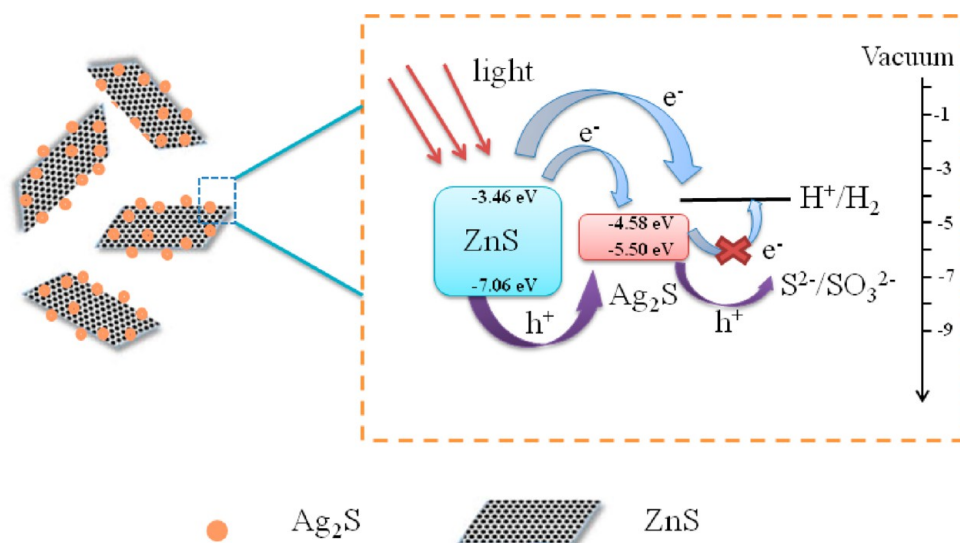
Figure 7. Schematic diagram of the porous ZnS:Ag$_2$S nanostructures for H$_2$ evolution.

9082

dx.doi.org/10.1021/am5020953 | ACS Appl. Mater. Interfaces 2014, 6, 9078−9084

better H$_2$ generation rates than those of the pure ZnS nanosheets and other ZnS:Ag$_2$S nanostructures.

3. CONCLUSIONS

In this work, porous ZnS:Ag$_2$S nanostructures have been prepared by a simple ion-exchange method. With different amounts of Ag$_2$S in the products, the porous nanostructures exhibit different pore sizes. Ag$_2$S acts as a hole-transfer medium, which would accelerate separation of the electrons and holes, thus enhancing the H$_2$ generation rate. This study shows that the amount of Ag$_2$S is also a key factor for H$_2$ generation. With the largest amounts of Ag$_2$S, the gas generation rate is low. The ZnS:Ag$_2$S porous nanocomposite (ZnS:Ag$_2$S-2) exhibits a good H$_2$ evolution rate of 104.9 μmol/h/g without a platinum cocatalyst. These results further indicate that surface modification is crucial to the photocatalytic activity of the ZnS nanosheets.

■ ASSOCIATED CONTENT

Ⓢ Supporting Information

Preparation of ZnS(en)$_{0.5}$ precursors, SEM and TEM images of Zn(en)$_{0.5}$S precursors, EDS spectra of ZnS, ZnS:Ag$_2$S-1, ZnS:Ag$_2$S-2, and ZnS:Ag$_2$S-8 nanostructures, elemental mapping of ZnS:Ag$_2$S-2 nanosheets, and SEM image of ZnS:Ag$_2$S-2 after photocatalytic testing. This material is available free of charge via the Internet at http://pubs.acs.org.

■ AUTHOR INFORMATION

Corresponding Author
*Tel.: +852-34427826. E-mail: apcslee@cityu.edu.hk.
Notes
The authors declare no competing financial interest.

■ ACKNOWLEDGMENTS

■ REFERENCES

(1) Sung, T. K.; Kang, J. H.; Jang, D. M.; Myung, Y.; Jung, G. B.; Kim, H. S.; Jung, C. S.; Cho, Y. J.; Park, J.; Lee, C.-L. CdSSe Layer-Sensitized TiO$_2$ Nanowire Arrays as Efficient Photoelectrodes. *J. Mater. Chem.* **2011**, *21*, 4553−4561.

(2) Su, J. Z.; Guo, L. J.; Bao, N. Z.; Grimes, C. A. Nanostructured WO$_3$/BiVO$_4$ Heterojunction Films for Efficient Photoelectrochemical Water Splitting. *Nano Lett.* **2011**, *11*, 1928−1933.

(3) Zong, X.; Han, J. F.; Ma, G. J.; Yan, H. J.; Wu, G. P.; Li, C. Photocatalytic H$_2$ Evolution on CdS Loaded with WS$_2$ as Cocatalyst under Visible Light Irradiation. *J. Phys. Chem. C* **2011**, *115*, 12202−12208.

(4) Kargar, A.; Jing, Y.; Kim, S. J.; Riley, C. T.; Pan, X. Q.; Wang, D. L. ZnO/CuO Heterojunction Branched Nanowires for Photo-electrochemical Hydrogen Generation. *ACS Nano* **2013**, *7*, 11112−11120.

(5) Shen, Z. Y.; Chen, G.; Wang, Q.; Yu, Y. G.; Zhou, C.; Wang, Y. Sonochemistry Synthesis and Enhanced Photocatalytic H$_2$-Production Activity of Nanocrystals Embedded in CdS/ZnS/In$_2$S$_3$ Microspheres. *Nanoscale* **2012**, *4*, 2010−2017.

(6) Zhou, W. J.; Yin, Z. Y.; Du, Y. P.; Huang, X.; Zeng, Z. Y.; Fan, Z. X.; Liu, H.; Wang, J. Y.; Zhang, H. Synthesis of Few-Layer MoS$_2$ Nanosheet-Coated TiO$_2$ Nanobelt Heterostructures for Enhanced Photocatalytic Activities. *Small* **2013**, *9*, 140−147.

(7) Hou, Y.; Zuo, F.; Dagg, A.; Feng, P. Y. Visible Light-Driven α-Fe$_2$O$_3$ nanorod/graphene/BiV$_{1−x}$Mo$_x$O$_4$ Core/Shell Heterojunction Array for Efficient Photoelectrochemical Water Splitting. *Nano Lett.* **2012**, *12*, 6464−6473.

(8) Xiang, Q. J.; Yu, J. G.; Jaroniec, M. Preparation and Enhanced Visible-Light Photocatalytic H$_2$-Production Activity of Graphene/C$_3$N$_4$ Composites. *J. Phys. Chem. C* **2011**, *115*, 7355−7363.

(9) Chen, X. B.; Shen, S. H.; Guo, L. J.; Mao, S. S. Semiconductor-Based Photocatalytic Hydrogen Generation. *Chem. Rev.* **2010**, *110*, 6503−6570.

(10) Wang, G. M.; Wang, H. Y.; Ling, Y. C.; Tang, Y. C.; Yang, X. Y.; Fitzmorris, R. C.; Wang, C. C.; Zhang, J. Z.; Li, Y. Hydrogen-Treated TiO$_2$ Nanowire Arrays for Photoelectrochemical Water Splitting. *Nano Lett.* **2011**, *11*, 3026−3033.

(11) Li, K.; Chai, B.; Peng, T. Y.; Mao, J.; Zan, L. Preparation of AgIn$_5$S$_8$/TiO$_2$ Heterojunction Nanocomposite and its Enhanced Photocatalytic H$_2$ Production Property under Visible Light. *ACS Catal.* **2013**, *3*, 170−177.

(12) Yin, Z. Y.; Wang, Z.; Du, Y. P.; Qi, X. Y.; Huang, Y. Z.; Xue, C.; Zhang, H. Full Solution-Processed Synthesis of All Metal Oxide-Based Tree-Like Heterostructures on Fluorine-Doped Tin Oxide for Water Splitting. *Adv. Mater.* **2012**, *24*, 5374−5378.

(13) Zhang, J. Y.; Wang, Y. H.; Jin, J.; Zhang, J.; Lin, Z.; Huang, F.; Yu, J. G. Efficient Visible-Light Photocatalytic Hydrogen Evolution and Enhanced Photostability of Core/Shell CdS/g-C$_3$N$_4$ Nanowires. *ACS Appl. Mater. Interfaces* **2013**, *5*, 10317−10324.

(14) Huang, X.; Zeng, Z. Y.; Bao, S. Y.; Wang, M. F.; Qi, X. Y.; Fan, Z. X.; Zhang, H. Solution-Phase Epitaxial Growth of Noble Metal Nanostructures on Dispersible Single-Layer Molybdenum Disulfide Nanosheets. *Nat. Commun.* **2013**, *4*, 1444.

(15) Lin, H. Y.; Chen, Y. F.; Chen, Y. W. Water Splitting Reaction on NiO/InVO$_4$ under Visible Light Irradiation. *Int. J. Hydrogen Energy* **2007**, *32*, 86−92.

(16) Zong, X.; Yan, H. J.; Wu, G. P.; Ma, G. J.; Wen, F. Y.; Wang, L.; Li, C. Enhancement of Photocatalytic H$_2$ Evolution on CdS by Loading MoS$_2$ as Cocatalyst under Visible Light Irradiation. *J. Am. Chem. Soc.* **2008**, *130*, 7176−7177.

(17) Huang, X.; Zeng, Z. Y.; Zhang, H. Metal Dichalcogenide Nanosheets: Preparation, Properties and Applications. *Chem. Soc. Rev.* **2013**, *42*, 1934−1946.

(18) Yan, H.; Yang, J.; Ma, G.; Wu, G.; Zong, X.; Lei, Z.; Shi, J.; Li, C. Visible-Light-Driven Hydrogen Production with Extremely High Quantum Efficiency on Pt−PdS/CdS Photocatalyst. *J. Catal.* **2009**, *266*, 165−168.

(19) Bao, N.; Shen, L.; Takata, T. Self-Templated Synthesis of Nanoporous CdS Nanostructures for Highly Efficient Photocatalytic Hydrogen Production under Visible Light. *Chem. Mater.* **2008**, *20*, 110−117.

(20) Sano, T.; Kutsuna, S.; Negishi, N.; Takeuchi, K. Effect of Pd-Photodeposition over TiO$_2$ on Product Selectivity in Photocatalytic Degradation of Vinyl Chloride Monomer. *J. Mol. Catal. A: Chem.* **2002**, *189*, 263−270.

(21) Yu, J. G.; Yang, B.; Cheng, B. Noble-Metal-Free Carbon Nanotube-Cd$_{0.1}$Zn$_{0.9}$S Composites for High Visible-Light Photo-catalytic H$_2$-Production Performance. *Nanoscale* **2012**, *4*, 2670−2677.

(22) Mukherji, A.; Seger, B.; Lu, G. Q.; Wang, L. Z. Nitrogen Doped Sr$_2$Ta$_2$O$_7$ Coupled with Graphene Sheets as Photocatalysts for Increased Photocatalytic Hydrogen Production. *ACS Nano* **2011**, *5*, 3483−3492.

(23) Xiang, Q. J.; Yu, J. G.; Jaroniec, M. Synergetic Effect of MoS$_2$ and Graphene as Cocatalysts for Enhanced Photocatalytic H$_2$ Production Activity of TiO$_2$ Nanoparticles. *J. Am. Chem. Soc.* **2012**, *134*, 6575−6578.

(24) Zhu, M. S.; Li, Z.; Xiao, B.; Lu, Y. T.; Du, Y. K.; Yang, P.; Wang, X. M. Surfactant Assistance in Improvement of Photocatalytic Hydrogen Production with the Porphyrin Noncovalently Function-alized Graphene Nanocomposite. *ACS Appl. Mater. Interfaces* **2013**, *5*, 1732−1740.

9083

dx.doi.org/10.1021/am5020953 | *ACS Appl. Mater. Interfaces* 2014, 6, 9078−9084

(25) Huang, X.; Qi, X. Y.; Boey, F.; Zhang, H. Graphene-Based Composites. *Chem. Soc. Rev.* **2012**, *41*, 666−686.

(26) Huang, L.; Yang, J. H.; Wang, X. L.; Han, J. F.; Han, H. X.; Li, C. Effects of Surface Modification on Photocatalytic Activity of CdS Nanocrystals Studied by Photoluminescence Spectroscopy. *Phys. Chem. Chem. Phys.* **2013**, *15*, 553−560.

(27) Zhong, X. H.; Feng, Y. Y.; Zhang, Y. L.; Gu, Z. Y.; Zou, L. A Facile Route to Violet- to Orange-Emitting $Cd_xZn_{1−x}Se$ Alloy Nanocrystals via Cation Exchange Reaction. *Nanotechnology* **2007**, *18*, 385606.

(28) Yang, J.; Zhou, Y. L.; Zheng, S. L.; Liu, X. F.; Qiu, X. H.; Tang, Z. Y.; Song, R.; He, Y. J.; Ahn, C. W.; Kim, J. W. Self-Reorganization of CdTe Nanoparticles into Near-Infrared $Hg_{1−x}Cd_xTe$ nanowire networks. *Chem. Mater.* **2009**, *21*, 3177−3182.

(29) Lubeck, C. R.; Han, T. Y. J.; Gash, A. E.; Satcher, J. H.; Doyle, F. M. Synthesis of Mesostructured Copper Sulfide by Cation Exchange and Liquid-Crystal Templating. *Adv. Mater.* **2006**, *18*, 781−784.

(30) Luther, J. M.; Zheng, H. M.; Sadtler, B.; Alivisatos, A. P. Synthesis of PbS nanorods and other Ionic Nanocrystals of Complex Morphology by Sequential Cation Exchange Reactions. *J. Am. Chem. Soc.* **2009**, *131*, 16851−16857.

(31) Xu, J.; Luan, C. Y.; Tang, Y. B.; Chen, X.; Zapien, J. A.; Zhang, W.-J.; Kwong, H.-L.; Meng, X.-M.; Lee, S.-T.; Lee, C.-S. Low-Temperature Synthesis of $CuInSe_2$ Nanotube Array on Conducting Glass Substrates for Solar Cell Application. *ACS Nano* **2010**, *4*, 6064−6070.

(32) Xu, J.; Yang, X.; Wang, H. K.; Chen, X.; Luan, C. Y.; Xu, Z. X.; Lu, Z. Z.; Roy, V. A. L.; Zhang, W. J.; Lee, C.-S. Arrays of ZnO/$Zn_xCd_{1−x}Se$ Nanocables: Band Gap Engineering and Photovoltaic Applications. *Nano Lett.* **2011**, *11*, 4138−4143.

(33) Zhu, Y. F.; Fan, D. H.; Shen, W. Z. Chemical Conversion Synthesis and Optical Properties of Metal Sulfide Hollow Microspheres. *Langmuir* **2008**, *24*, 11131−11136.

(34) Yu, J. G.; Zhang, J.; Liu, S. W. Ion-Exchange Synthesis and Enhanced Visible-Light Photoactivity of CuS/ZnS Nanocomposite Hollow Spheres. *J. Phys. Chem. C* **2010**, *114*, 13642−13649.

(35) Zhang, J.; Yu, J. G.; Zhang, Y. M.; Li, Q.; Gong, J. R. Visible Light Photocatalytic H_2-Production Activity of CuS/ZnS Porous Nanosheets Based on Photoinduced Interfacial Charge Transfer. *Nano Lett.* **2011**, *11*, 4774−4779.

(36) Yu, Y. F.; Zhang, J.; Wu, X.; Zhao, W. W.; Zhang, B. Nanoporous Single-Crystal-Like $Cd_xZn_{1−x}S$ Nanosheets Fabricated by the Cation-Exchange Reaction of Inorganic−Organic Hybrid ZnS−Amine with Cadmium Ions. *Angew. Chem., Int. Ed.* **2012**, *51*, 897−900.

(37) Chaudhuri, R. G.; Paria, S. Optical Properties of Double-Shell Hollow ZnS−Ag_2S Nanoparticles. *J. Phys. Chem. C* **2013**, *117*, 23385−23390.

(38) Shen, S. L.; Zhang, Y. J.; Peng, L.; Du, Y. P.; Wang, Q. B. Matchstick-Shaped Ag_2S−ZnS Heteronanostructures Preserving both UV/Blue and Near-Infrared Photoluminescence. *Angew. Chem., Int. Ed.* **2011**, *50*, 7115−7118.

(39) Zhang, H. L.; Wei, B.; Zhu, L.; Yu, J. H.; Sun, W. J.; Xu, L. L. Cation Exchange Synthesis of ZnS−Ag_2S Microspheric Composites with Enhanced Photocatalytic Activity. *Appl. Surf. Sci.* **2013**, *270*, 133−138.

(40) Liu, J. Y.; Guo, Z.; Meng, F. L.; Luo, T.; Li, M. Q.; Liu, J. H. Novel Porous Single-Crystalline ZnO Nanosheets Fabricated by Annealing $ZnS(en)_{0.5}$ (en = ethylenediamine) Precursor. Application in a Gas Sensor for Indoor Air Contaminant Detection. *Nanotechnology* **2009**, *20*, 125501.

(41) Ouyang, S. X.; Tong, H.; Umezawa, N.; Cao, J. Y.; Li, P.; Bi, Y. P.; Zhang, Y. J.; Ye, J. H. Surface-Alkalinization-Induced Enhancement of Photocatalytic H_2 Evolution over $SrTiO_3$-Based Photocatalysts. *J. Am. Chem. Soc.* **2012**, *134*, 1974−1977.

(42) Ni, Y. H.; Cao, X. F.; Hu, G. Z.; Yang, Z. S.; Wei, X. W.; Chen, Y. H.; Xu, J. Preparation, Conversion, and Comparison of the Photocatalytic and Electrochemical Properties of $ZnS(en)_{0.5}$, ZnS, and ZnO. *Cryst. Growth Des.* **2007**, *7*, 280−285.

(43) Park, J.; Zheng, H. M.; Jun, Y.-W.; Alivisatos, A. P. Heteroepitaxial Anion Exchange Yields Single-Crystalline Hollow Nanoparticles. *J. Am. Chem. Soc.* **2009**, *131*, 13943−13945.

(44) Yin, Y. D.; Erdonmez, C. K.; Cabot, A.; Hughes, S.; Alivisatos, A. P. Colloidal Synthesis of Hollow Cobalt Sulfide Nanocrystals. *Adv. Funct. Mater.* **2006**, *16*, 1389−1399.

(45) Xu, J.; Tang, Y. B.; Zhang, W. X.; Lee, C. S.; Yang, Z. H.; Lee, S. T. Fabrication of Architectures with Dual Hollow Structures: Arrays of Cu_2O Nanotubes Organized by Hollow Nanospheres. *Cryst. Growth Des.* **2009**, *9*, 4524−4528.

(46) Shuai, X. M.; Shen, W. Z. A Facile Chemical Conversion Synthesis of ZnO/ZnS Core/Shell Nanorods and Diverse Metal Sulfide Nanotubes. *J. Phys. Chem. C* **2011**, *115*, 6415−6422.

(47) Reber, J. F.; Rusek, M. Photochemical Hydrogen Production with Platinized Suspensions of Cadmium Sulfide and Cadmium Zinc Sulfide Modified by Silver Sulfide. *J. Phys. Chem.* **1986**, *90*, 824−834.